ORIGINAL RESEARCH ARTICLE

On the Mechanism of Steel Homogenization *via* Rare Earth Addition: Experimental Characterization and Numerical Simulation

YANFEI CAO, YANGYANG MIAO, DIANZHONG LI, YUN CHEN, PAIXIAN FU, HONGWEI LIU, XIUHONG KANG, HANGHANG LIU, and CHEN SUN

Macrosegregation is one of the most typical defects during solidification which greatly limits the mechanical properties of the key steel components. Oxygen and its inclusion have been considered to cause the compositional heterogeneity in solidifying steel besides the thermo-solutal convection. However, it is still not clear how to robustly reduce the oxygen and inclusion and consequently macrosegregation in widely used steels. Here, we reported the mechanism to homogenize the steel *via* Rare Earth (RE) addition. A series of experimental characterizations of 3-ton bearing steel ingots demonstrated that RE is able to decrease the oxygen content and inclusions to a lower level than the conventional Al-deoxidation process. The common oxide and sulfide can be modified into spherical or ellipsoidal RE_2O_2S with a dispersed distribution. The multi-component/multi-phase macrosegregation simulations show that the larger size and population of RE_2O_2S are required to trigger channel segregation in RE steel due to its higher density compared to the alumina-based inclusions. The theoretical calculation reveals that the critical oxygen content in RE steel to eliminate channel segregation is dramatically increased into 20 ppm, which indicates a lower risk of destabilization of mushy zone and initiation of channel segregation in RE steel. In addition, the global macrosegregation severity is reduced in RE steel. Such conclusion is fully validated in larger 9.5-ton and 100-ton steel ingots. In terms of the interaction between inclusion motion, fluid flow, and solidification, this study elucidates the mechanism of RE to reduce macrosegregation for the first time, and highlights an economic, common, and controllable method to fabricate homogenized steel by RE addition.

I. INTRODUCTION

MACROSEGREGATION is the most common casting defect of steel ingots, attracting the widespread attention of scientists and engineers due to its irreparable nature by the sequential processes such as forging, rolling, and heat treatment. It is defined as the non-uniform or heterogeneous distributions of solutal elements in the macro-scale region. Generally, it is considered to be induced by the solutal partitioning in the solid–liquid interface and the relative motion between solid and liquid phases during solidification. According to the classical theory, the long-range movement of solute is caused by three known forces: the buoyancy force of the natural thermo-solutal convection, the solid movement force of settling or flotation, and the shrinkage force of the volume contraction during solidification.

During the past decades, the advanced macrosegregation models such as multi-phase/multi-scale/multi-component models have been established based on the above classical theory.[1–11] Yet, some differences between experimental and simulation results always exist, and it is faintly ascribed to the inputs of complex macrosegregation models, such as the coarsened computing grid, the uncertain material parameters, and the simplification of auxiliary models.[8,12,13] On the other hand, the distinct chemical inhomogeneity in large steel

YANFEI CAO, DIANZHONG LI, YUN CHEN, PAIXIAN FU, HONGWEI LIU, XIUHONG KANG, HANGHANG LIU, and CHEN SUN are with the Shenyang National Laboratory for Materials Science, Institute of Metal Research, Chinese Academy of Sciences, Wenhua Road No. 72, Shenyang 110016, P.R. China. Contact e-mail: dzli@imr.ac.cn YANGYANG MIAO is with the Shenyang National Laboratory for Materials Science, Institute of Metal Research, Chinese Academy of Sciences and also with the School of Materials Science and Engineering, University of Science and Technology of China, Hefei 230026, P.R. China.

ingots in practice cannot be effectively controlled by using the traditional technologies such as rapid cooling, mechanical stirring, local vibration, and so on. Hence, the above dilemmas have been stimulating the exploration of the other driving force and control method of macrosegregation in steel. Recently, it was found that oxygen and its inclusion are the origin of channel segregation, the most notorious and undesirable type of macrosegregation in solidifying steels.[14] The sufficient volume fraction of oxide-based inclusions with appropriate sizes can enhance the local flow, destabilize the mushy zone, and eventually dominate the channel segregation formation. Meanwhile, the channel segregation can be reduced obviously and even eliminated as the oxygen content is controlled almost below 10 ppm in practice. It highlights the importance of low-oxygen purifying treatment and inclusion modification (*e.g.*, size, quantity and composition) during the refining and solidification processes to suppress the severity of macrosegregation. However, to date, it is still not clear how to reduce and even eliminate the channel segregation by an economic, simple, common, and controllable method.

Owing to the strong chemical reactivity of Rare Earth (RE) elements, it is the best potential choice for deoxidization in the steel melt. Actually, RE steel has been recognized as one of revolutionary technologies because of their superior properties of toughness, plasticity, heat-resistant and corrosion-resistant as well as wear-resistant behaviors, consequently leading to the flourishing situation and the wide application of RE in steelmaking in 1980s.[15–17] Besides the micro-alloying effect of RE with its larger atomic radius,[18–20] two other superior natures of RE in steel should be stressed here: (1) effective purifications in deoxidization and desulfurization, and (2) apparent modification of inclusions from the hard inclusions to relatively fine, and soft RE-oxy-sulfide. Based on the mentioned formation mechanism of macrosegregation by inclusion flotation, these two natures above are undoubtedly fascinating in controlling and reducing channel segregation. Unfortunately, the influence and mechanism of RE addition on macrosegregation have been neglected for a long period though the inclusion modification and micro-alloying effects of RE addition in steels have been focused on.[21–24]

To illustrate the characteristics of inclusion modification and the resulting difference of macrosegregation *via* RE addition, the multi-scale characterization techniques are applied besides the common methods of optical microscope (OM), scanning electron microscope (SEM), electron probe micro analyzer (EPMA), and transmission electron microscope (TEM). For instance, a large-scale measurement system of ASPEX Explorer (FEI company), combining the SEM and EDX, was used to scan the inclusions in the current study considering its unique advantages such as high accuracy, efficiency, and more collecting points. Besides, X-ray microtomography technique (3D Micro-CT)[25–27] was also applied to analyze the size, number, and volume fraction of inclusions in bearing steels with and without RE metals in three-dimensional space. Based on a series of experimental characterizations, an Euler–Lagrange multi-component macrosegregation model encompassing the inclusion flotation was built to elucidate the effects of RE addition on the convection, solidification, and the final macrosegregation in industrial ingots. Finally, the feasibility to improve the compositional homogenization *via* RE addition was verified and extended to the larger 9.5-ton and 100-ton steel ingots which are used to produce gearing and shaft, respectively.

II. INCLUSION MODIFICATION BY RE ADDITION IN 3-TON BEARING STEEL INGOTS

A. *Experimental Procedure*

3-Ton cylinder ingots of bearing steel with RE addition were first prepared and synthesized in a cast iron mold. The main chemical compositions (wt pct) of the ingot are C 1.0, Si 0.25, Cr 1.5, Mn 0.35, S 0.003, and Fe balanced. The ingot dimensions and shape are illustrated in Figure 1(a). An insulation sleeve with a thickness of 240 mm was inserted at the circumference of the hot top mold. The top of the riser was covered by a 40-mm-thick layer of covering flux. The steel was melted at 1823 K by an Electric Furnace (EF), refined with ladle furnace (LF) refining and Ruhrstahl Heraeus (RH) vacuum treatment (LF + RH), and then poured at 1773 K in air. Before being poured, the steel melt was purified by RE treatment with 0.019 wt pct La + Ce mischmetal addition (Ce/La ≈ 2). The solidified as-cast ingots were cut in half along the longitudinal axis for the detailed measurement and characterization of inclusions. Meanwhile, the referred steel ingots with the same process and chemical compositions were also produced and compared, but the RE addition was not applied.

In order to accurately detect the distribution, type, and quantity of inclusions, a large-scale characterization technique of ASPEX was used. First, three slices of $50 \times 50 \times 15$ mm^3 were cut at the mid-radius at the bottom, middle, and top of the ingot, respectively, as shown in Figure 1(b). After being ground and polished, samples with a size of $10 \times 10 \times 10$ mm in each slice were placed on the platform of the ASPEX scanning system (EXplorer 4 analyzer) with a working accelerating voltage of 20 kV. The applied resolution is 1 μm and the scanning area is 50 mm^2. Then, to reveal the modification and evolution details of inclusions by RE treatment, the characterizations were carried out by Nova NanoSEM 430 field emission gun SEM with EDX surface scanning and F20 TEM. In addition, to quantitatively measure the dimension, quantity, and morphology of inclusions in the three-dimensional space, cylindrical samples of $\Phi1 \times 10$ mm^2 were then observed by using X-ray microtomography technique (3D Micro-CT) under the lab-based Xradia Versa XRM-500 system.[28] The accelerating voltage and pixel size were 140 kV and 1.1 μm, respectively. In total, 1600 projected images with an exposure time of 4 seconds were recorded as the sample was rotated by 360 deg, and then they were reconstructed, processed, visualized, and
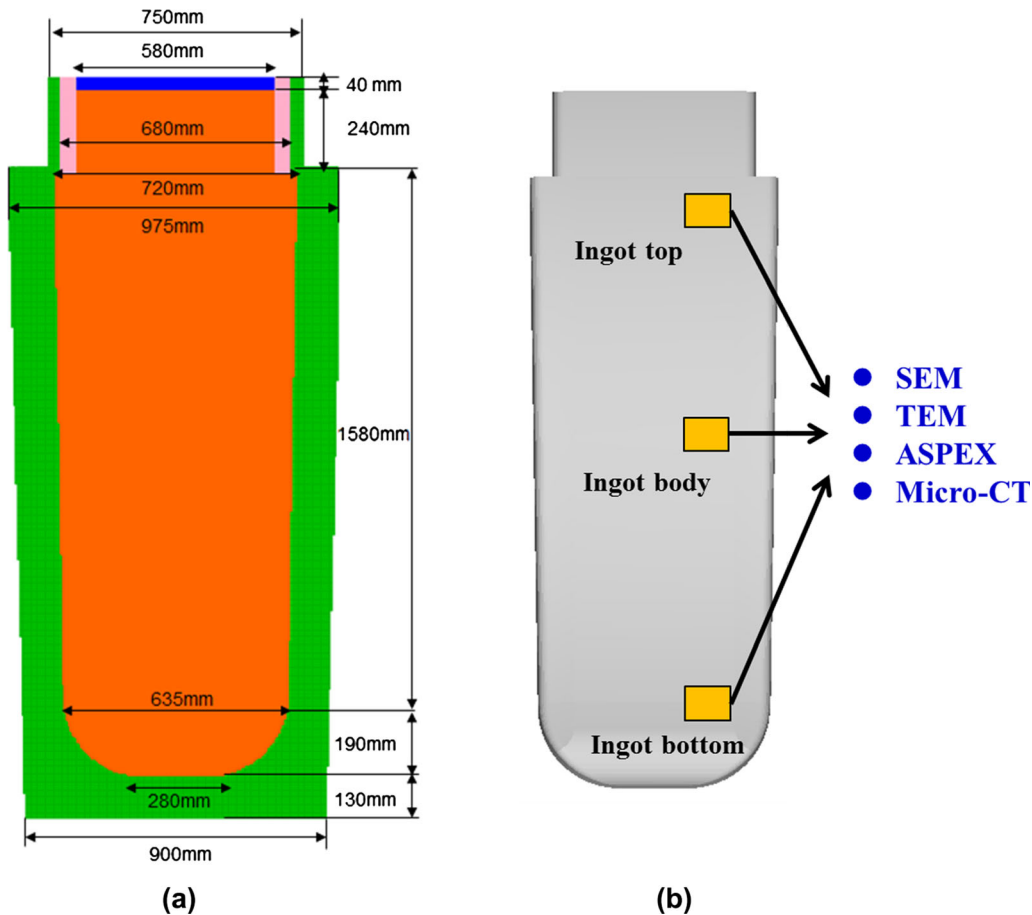
Fig. 1—The schematic and geometry (*a*) and the sample positions (*b*) of the 3-ton bearing steel ingot. The orange, pink, blue, and green regions in (a) denote ingot, insulation sleeve, covering flux, and iron mold, respectively (Color figure online).

computed using the software of Avizo fire. Considering the appropriate size of inclusions of 5–50 μm to induce the formation of channel segregation,[14] the current resolutions of 1 μm in 2D ASPEX and 1.1 μm in 3D Micro-CT are reasonable and the effect of inclusions below about 1 μm can be fully neglected considering our special focus on the formation of macrosegregation. Finally, the oxygen content in either case of RE addition or not was compared by chemical analysis to reveal its role in deoxidization. As a wider application and verification of RE in the reduction of macrosegregation, the chemical distribution of carbon in the other 9.5-ton and 100-ton steel ingots was finally determined quantitatively.

B. *Inclusion Measurement and Observation*

The main dimension and chemical composition of inclusions by RE-free treatment are shown in Table I. Eight types of inclusions are at least detected, of which the main large inclusions are alumina and its complex inclusions. During the tapping process of the EF furnace and LF refining process, Al chunks and particles were added into the steel melt to reduce the oxygen content, and Al inclusions form. S inclusions such as MnS are caused by the melting pig iron and manganese chunks during the tapping process of the EF furnace. Ca

inclusions are related to the addition of lime CaO in the steel melt to make slag to conduct de-phosphorization during EF and deoxidation and desulfurization during LF process, respectively. Mg inclusions mainly originate from the refractory material of ladle in which MgO–C brick is often applied in steelmaking. In terms of Ti inclusions, they mainly stem from the slag during EF and LF and the raw materials such as Fe alloy and Cr alloy. The detected total inclusions above 1 μm are 199, and the average and maximum diameters are 3.4 and 26.1 μm, respectively. By contrast, the inclusion features in the ingot with RE addition are listed in Table II. It shows that only 67 inclusions are detected in the top view of about 50 mm^2 of which the largest inclusion is 7.2 μm and the average size is 3.3 μm.

Though the average size of inclusions in both RE and RE-free steels is almost the same, the maximum inclusion size by RE treatment is much smaller compared to that in RE-free steel. In addition, the number of inclusions (> 1 μm) is dramatically decreased *via* RE treatment, and generally it is about 2.5 times larger in the RE-free ingot compared with that in the RE ingot. On one hand, it is caused by the deep deoxidation and desulfurization abilities of RE element (see Figure 3, below), which lowers the maximum inclusion size and the number of large inclusions (> 1 μm). On the other hand, owing to the good wetting ability between

Table I. The Main Inclusion Size d_p, Number n, and Composition Measured by ASPEX Device in RE-Free Steel

Composition	$d_{p\text{-ave}}$ (μm)	$d_{p\text{-max}}$ (μm)	$n_{1-3~\mu\text{m}}$	$n_{3-5~\mu\text{m}}$	$n_{5-10~\mu\text{m}}$	$n_{10-20~\mu\text{m}}$	$n_{20-50~\mu\text{m}}$
Al_2O_3	5	17.9	8	6	5	2	0
MnS	2.3	7.6	52	4	1	0	0
CaO–MnS	2.3	3.2	5	1	0	0	0
MgO–Al_2O_3–MnS	3.4	7.3	4	3	1	0	0
SiO_2	8.1	9.9	0	0	2	0	0
TiO_2	4.2	9.2	4	10	3	0	0
CaS–Al_2O_3–MnS	3.7	26.1	29	26	9	0	1

Table II. The Main Inclusion Size d_p, Number n, and Composition Measured by ASPEX Device in RE Steel

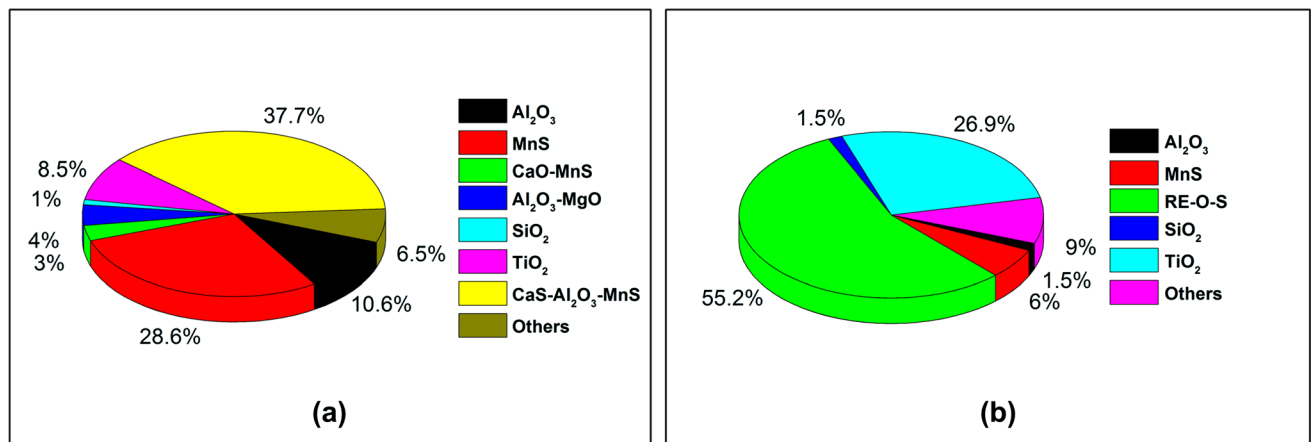| Composition	$d_{p\text{-ave}}$ (μm)	$d_{p\text{-max}}$ (μm)	$n_{1-3~\mu\text{m}}$	$n_{3-5~\mu\text{m}}$	$n_{5-10~\mu\text{m}}$	$n_{10-20~\mu\text{m}}$	$n_{20-50~\mu\text{m}}$
Al_2O_3	2.1	2.1	1	0	0	0	0
MnS	1.6	2.3	4	0	0	0	0
RE–O–S	2.6	5.6	28	7	2	0	0
SiO_2	4	4	0	1	0	0	0
TiO_2	5	7.2	4	7	7	0	0

Fig. 2—The percentage of different inclusion types in the RE-free (*a*) and RE (*b*) steels.

RE-type inclusions and steel melt (actually, the equilibrium contact wetting angle of Fe–RE_2O_3 is only half of Fe–Al_2O_3),[21] they are less prone to converge each other and grow up.

The quantitative statistical results of inclusion distribution with different compositions are further summarized in Figure 2. For RE-free steel, the main inclusion types are Al_2O_3-based inclusion and MnS. They are replaced by RE–O–S inclusions after RE treatment. Obviously, it is caused by the strong binding capacity between RE and O and S. Additionally, it seems that there is a distinct difference in the percentage of TiO_2 in Figure 2, but it is just caused by the large difference of the total inclusion number in two cases. Actually, their real numbers of TiO_2 are almost the same in RE-free and RE steels (References 17, 18 as referred in Tables I and II, respectively). In terms of MnS and SiO_2, due to the strong affinity among RE and O and S, RE–O–S forms easily and it is as high as 55.2 pct in the RE steel ingot. In such situation, massive O and S are consumed

by RE. Consequently, less S forms MnS, and less O forms SiO_2. In addition, the lower total oxygen content (see below) also reduces the contents of SiO_2 and the large MnS nucleated in the surface of alumina via RE treatment.

Figure 3 shows the effect of RE addition on the final oxygen content at different positions of steel ingot schematized in Figure 1(b). The oxygen contents in all these samples of RE steel ingots are smaller than the RE-free ingots, and its average value is lowered to 4.7 ppm from 5.5 ppm in RE-free ingot. That is, though the density of RE inclusion is much larger than the common Al_2O_3, they still float towards the slag when both RH and solidification times are sufficiently long after RE addition.

The SEM and EDX analyses of the typical inclusions with a higher resolution are shown in Figure 4. It reveals that the main inclusion types in RE-free ingots are alumina, MnS, and their complex inclusions, which are consistent with the ASPEX analysis. Generally, the

alumina, together with MgO or CaO, is surrounded by the manganese sulfide and acts as the nucleation site of the latter, and thus they always coexist. Yet, when RE element is added into the steel melt, most of inclusions become RE-type inclusions and are rich in oxygen and sulfur, as shown in Figure 4(b). The morphology of inclusions has also become spherical or ellipsoidal from the common complex shape.
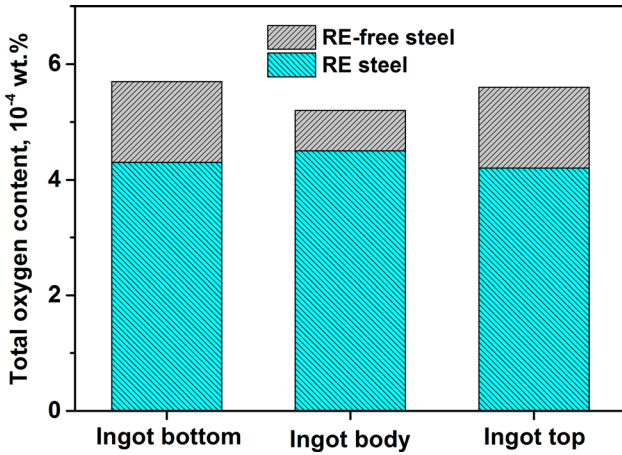

Fig. 3—The comparison of total oxygen content between RE-free and RE steels.

In addition, the chemical structure of such RE–O–S inclusion was further characterized by the TEM analysis, see Figure 5. It shows that the typical RE-type inclusion is RE_2O_2S such as Ce_2O_2S (or La_2O_2S), and agglomeration phenomenon is not observed because of its low interfacial tension in steel melt.[29] It should be stressed that, although it always appears as the typical composition of Ce_2O_2S in this work, its morphology, chemical composition, and type of RE-type inclusions vary with the modification of RE and S/O ratio.[22,30] For instance, as the binding capacity of Ce oxides and oxygen is greater than that of aluminum and oxygen, the liquid steel first produces $CeAlO_3$ when Ce content is small, and the reaction is given as follows:

$$[Ce] + [Al] + 3[O] = CeAlO_3 \qquad [1]$$
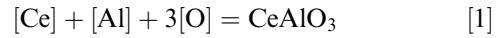
Reactions (2) and (3) below occur when the amount of Ce increases, which can modify Al_2O_3 inclusions and also play a role of desulfurization. Ce aluminate, Ce oxide, Ce sulfur oxide, and Ce sulfide will appear in sequence based on the free energy calculations with Ce addition.

$$CeAlO_3 + [Ce] + [S] = [Al] + [O] + Ce_2O_2S \qquad [2]$$

$$[Ce] + [O] = Ce_2O_3 \qquad [3]$$
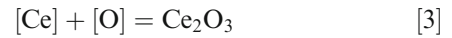
In terms of the formation of Ce_2O_2S, the following reaction of Eq. [4] occurs and its Gibbs free energy ΔG is listed in Eq. [5].
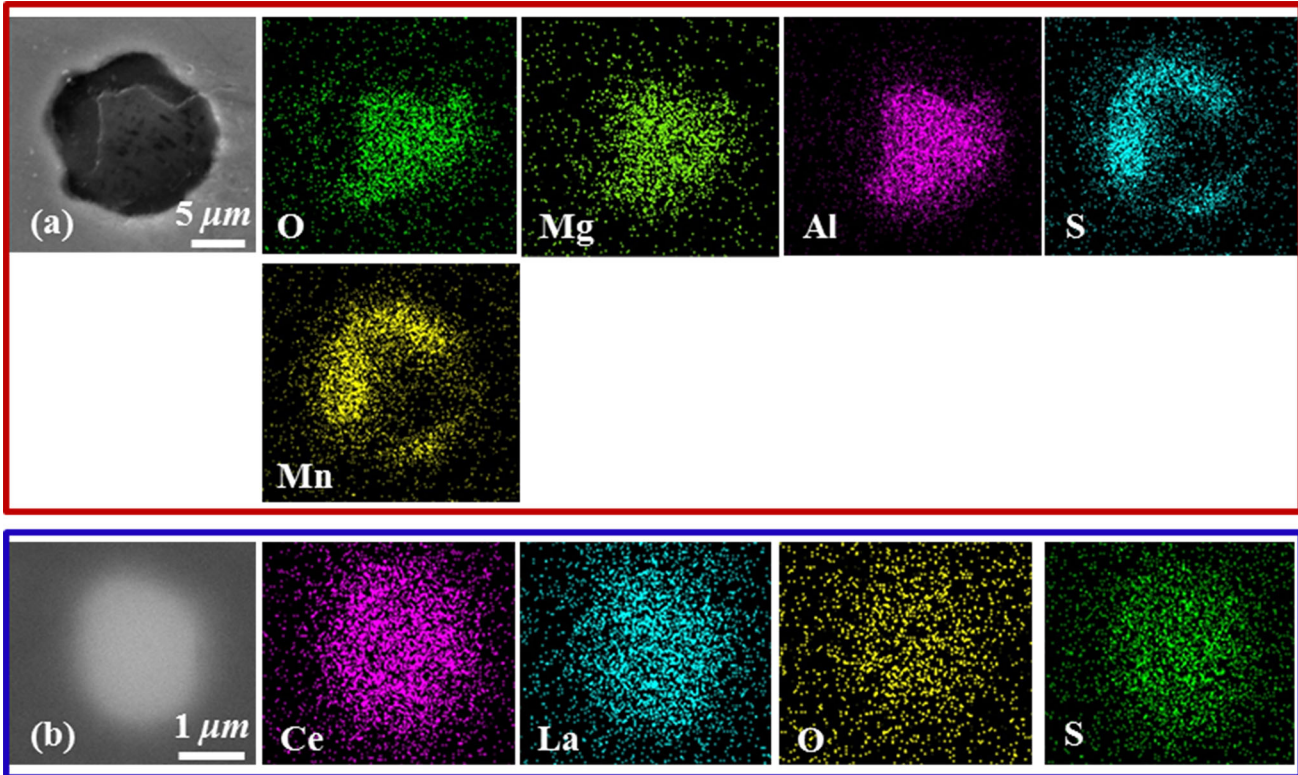

Fig. 4—The typical inclusion types and their composition in the RE-free (a) and RE (b) steels.
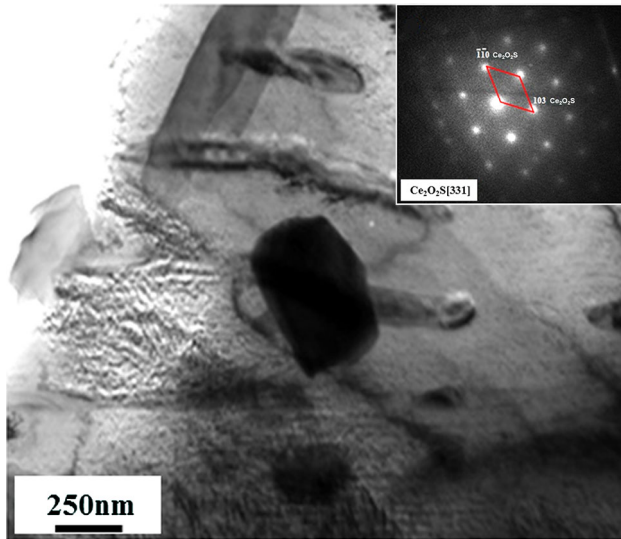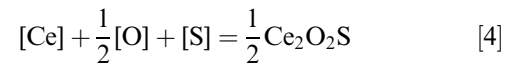
Fig. 5—The Ce$_2$O$_2$S inclusion morphology characterized by TEM in the RE steel, and its diffraction pattern is also superimposed.

$$[Ce] + \frac{1}{2}[O] + [S] = \frac{1}{2}Ce_2O_2S \qquad [4]$$

$$\Delta G = RT \ln J - RT \ln J^\theta \qquad [5]$$

$$\Delta G^\theta = -RT \ln J^\theta = -675700 + 165.50T \qquad [6]$$

$$J = \frac{1}{[Ce]^2 f_{Ce}^2 [O] f_O [S]^2 f_S^2}, \qquad [7]$$

where J is the equilibrium constant and superscript θ denotes standard state. R is the gas constant. f_{Ce}, f_O, and f_S are Henrian activity coefficients of Ce, O, and S, respectively. [Ce], [O], and [S] are mass fractions of Ce, O, and S, respectively. When replacing the activity coefficient by interaction coefficient, Eq. [7] can be
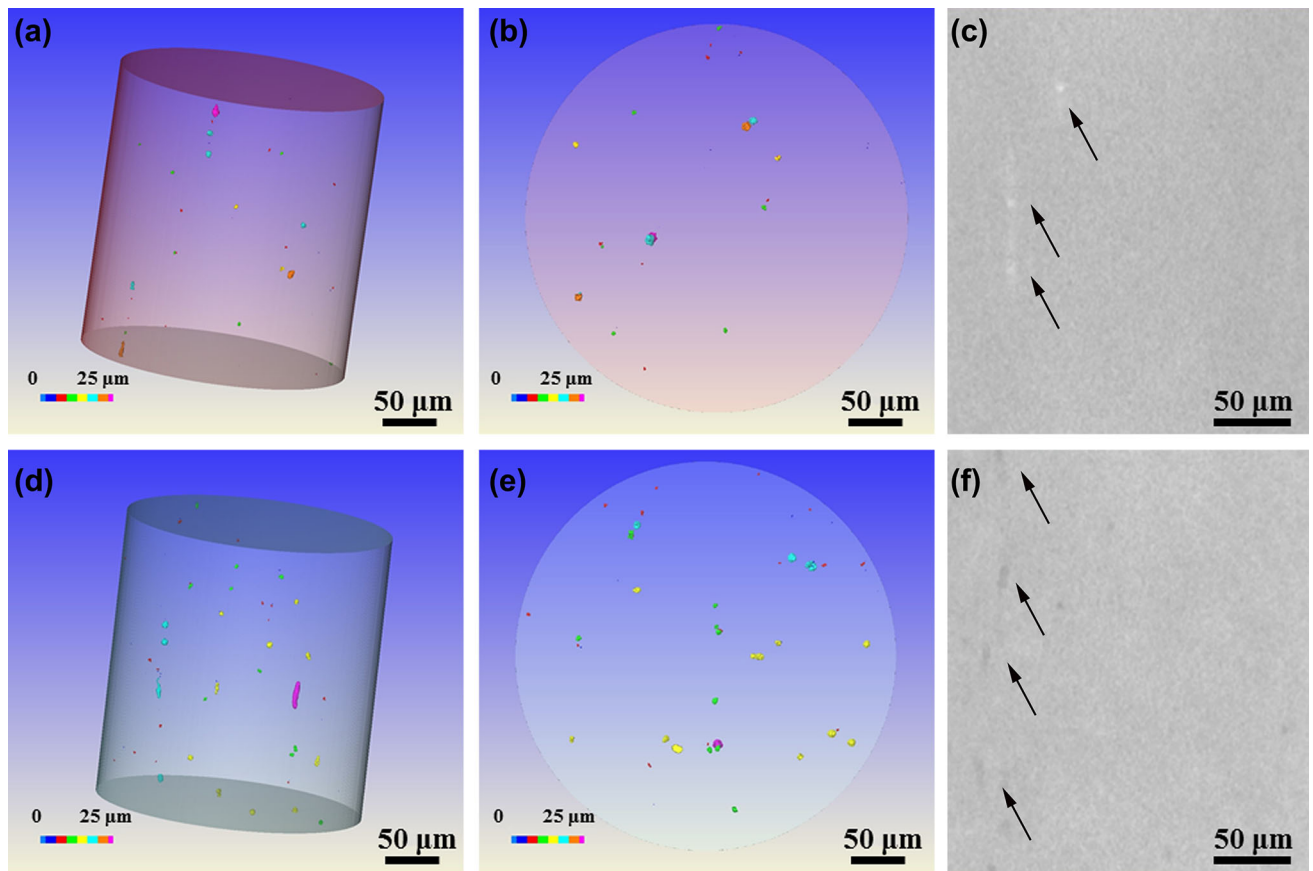

Fig. 6—The 3D distribution of inclusions by X-ray micro-CT technique in RE (a–c) and RE-free (d–f) steels. The constructed zone of (a) and (d) is Φ800 μm × 870 μm, and (b, e) and (c, f) are their transversal (color) and longitudinal (bitmap) slices, respectively. The different types of inclusions are marked by black arrows in (c) and (f) (Color figure online).

rewritten as follows:

$$\ln J = \ln \frac{1}{[\text{Ce}]^2[\text{O}][\text{S}]^2} - 2\sum e_{\text{Ce}}^w[w] - \sum e_{\text{O}}^w[w] \\ - 2\sum e_{\text{S}}^w[w],$$ [8]

where e, e, and e are interaction coefficients of Ce, O, and S by solute w with the weight percent $[w]$, respectively. Considering the interaction coefficients and the chemical compositions of the aimed steel,[22,31] ΔG is calculated to be -61963 J mol^{-1}, which sheds light on the reasonability of Ce$_2$O$_2$S inclusion in RE steel ingot owing to its much negative formation energy.

The 3D information of inclusions such as the morphology, distribution, and size is depicted in Figure 6. The 3D reconstructed region is $\Phi800 \times 870$ μm. The different colors represent the different equivalent volume diameters (each inclusion is considered as an equivalent sphere with a diameter of d_p) of inclusions. As identified by SEM and EDS above, RE-type inclusions are distributed dispersedly and appear as a spherical or ellipsoidal shape. But in the RE-free ingot, the inclusion morphology becomes complex and irregular. Owing to the larger density of RE element than Fe matrix, the contrast of RE-type inclusion becomes light and white (Figure 6(c)), which is completely different from the common gray alumina and manganese sulfide inclusions (Figure 6(f)).

The quantitative result of inclusions such as dimension and quantity by 3D Micro-CT technique is shown in Figure 7. In each size range, the inclusion number of RE steel becomes smaller compared to RE-free steel, and the maximum inclusion diameter also decreases to 21 from 34 μm. It should be noted that the sharp increment of inclusion size from 2D ASPEX to 3D Micro-CT analyses with the same resolution of about 1 μm is caused by their statistical methods.[32] In the 3D Micro-CT experiment, the 3D information can be revealed, and the large throughout inclusions in the

depth direction (see Figure 6) will significantly increase the dimension of inclusions. But in the 2D detection, only certain projection of inclusion can be observed, which causes the inaccurate evaluation and deviation. Yet, the difference in the absolute values in 2D and 3D will not influence the conclusion of the current research. That is, the common oxide and sulfide can be modified into the spherical or ellipsoidal RE$_2$O$_2$S, which tends to be dispersed in the melt during solidification. It in turn leads to a much finer inclusion size after solidification as shown in 2D and 3D analyses.

Based on the above characterization results, the RE addition in the steel melt can obviously decrease the number and size of the large inclusions. This will have a positive effect on the reduction of macrosegregation during solidification based on the mechanism of inclusion flotation-driven channel segregation. To obtain the interaction mechanism and detail between RE inclusion and solute transport, in the following sections, a series of simulations of the effect of different inclusions such as Al$_2$O$_3$ and Ce$_2$O$_2$S on the macrosegregation in industrial steel ingots are to be performed.

III. SIMULATION METHODOLOGY

Inclusion particles are considered to be distributed dispersedly in the melt at the beginning of solidification, and thus their motion characteristics are significantly distinct from the continuum phase.[28] Hence, here the multi-component macrosegregation model encompassing the inclusion flotation based on the classical continuum model is built and applied, in which the motions of liquid and solid inclusions are described using the multi-phase flow scheme within the Euler–Lagrange framework. The main conservation and auxiliary equations of continuum and dispersed phases are listed below.

A. Continuum Phase

Conservation of mass (Continuity):

$$\nabla \cdot \left(\vec{U} \right) = 0.$$ [9]

Conservation of solute:

$$\frac{\partial [C^j]}{\partial t} + \nabla \cdot \left(\vec{U} C_l^j \right) = 0$$ [10]

$$[C^j] = \int_0^{f_s} C_s^j \mathrm{d}\alpha + f_l C_l^j$$ [11]
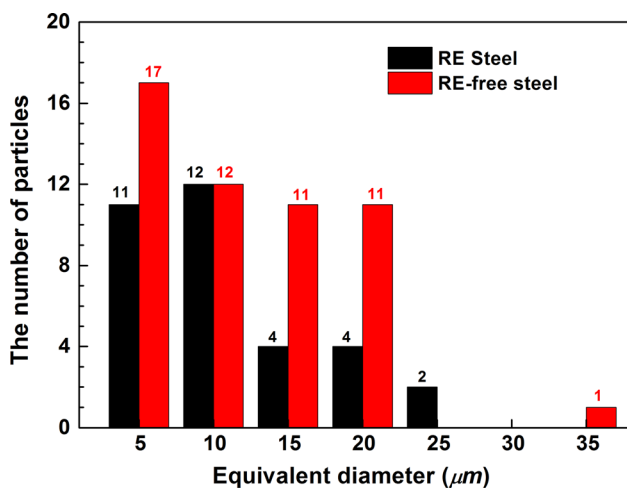
$$T_l = T_m + \sum_{j=1} m^j C_l^j.$$ [12]

Fig. 7—The statistical inclusion dimension and number by 3D X-ray micro-CT technique in RE and RE-free steels with the constructed zone of $\Phi800 \times 870$ μm.

Conservation of energy:

$$\frac{\partial(\rho H)}{\partial t} + \nabla \cdot \left(\rho c_p \overrightarrow{U} T + \rho \overrightarrow{U} \Delta H\right) = \nabla \cdot (\lambda \nabla T), \quad [13]$$

$$[pH] = f_s \rho_s h_s + f_l \rho_l h_l. \quad [14]$$

Conservation of momentum (x and y directions):

$$\frac{\partial(f_l \rho u)}{\partial t} + \nabla \cdot \left(\rho \overrightarrow{U} u\right) = -f_l \frac{\partial P}{\partial x} + \nabla \cdot (\mu_l \nabla(f_l u))$$
$$+ K_{sl}(\overline{u_p} - u) + \sum_{i=1} \left[K_{pl}^i \left(u_p^i - u\right)\right]$$
$$[15]$$

$$\frac{\partial(\rho f_l v)}{\partial t} + \nabla \cdot \left(\rho \overrightarrow{U} v\right) = -f_l \frac{\partial P}{\partial y} + \nabla \cdot (\mu_l \nabla(f_l v))$$
$$+ \rho \overrightarrow{g} f_l \left[\beta_T(T - T^*) + \sum_{j=1} \beta_C\left(C_l^j - C^{j*}\right)\right],$$
$$+ K_{sl}(\overline{v_p} - v) + \sum_{i=1} \left[K_{pl}^i \left(v_p^i - v\right)\right]$$
$$[16]$$

where $\overrightarrow{U} = f_l \overrightarrow{U_l}$ is the superficial velocity of liquid phase. K_{sl} ($K_{i\,pl}$) is the interfacial friction coefficient between the solid dendritic network (the ith inclusion particle) and the fluid phase,[28] which is modified from the Gidaspow correction[33]

$$K_{sl} = 150 \frac{f_s^2 \mu_l}{f_l d_s^2} \quad [17]$$

$$K_{pl}^i = \frac{3}{4} C_D \frac{f_p f_l \rho}{d_p} \left|v_p^i - v\right| f_l^{-2.65}, \quad [18]$$

where C_D is the drag coefficient and equal to $24/Re$ for spherical solid particles. To calculate the solid fraction, the same strategy was applied by solving the built high-order equation considering the energy and species conservations, thermodynamic equilibrium at the solid–liquid interface and microsegregation model.[34]

These governing equations are discretized on a staggered Cartesian mesh using uniform spaced grids. An explicit scheme of finite volume method is adopted to solve the coupled equations for temperature and concentration. The velocity–pressure coupling is realized using the SOLA algorithm to improve the computational efficiency considering the multi-phase complex system in the industrial steel ingot. As the calculation of liquid flow is accomplished in a time step, the motion of inclusion is tracked *via* the following procedures.

B. *Dispersed Phase*

1. *Velocity equations*

$$\frac{\mathrm{d}u_p^i}{\mathrm{d}t} = \frac{18\mu_l}{\rho_p d_p^2} \frac{C_D Re}{24} \left(u - u_p^i\right) \quad [19]$$

$$\frac{\mathrm{d}v_p^i}{\mathrm{d}t} = \frac{18\mu_l}{\rho_p d_p^2} \frac{C_D Re}{24} \left(v - v_p^i\right) + \frac{\overrightarrow{g}\,(\rho_p - \rho)}{\rho_p} \quad [20]$$

2. *Trajectory equations*

$$\frac{\mathrm{d}x^i}{\mathrm{d}t} = u_p^i, \quad \frac{\mathrm{d}y^i}{\mathrm{d}t} = v_p^i, \quad [21]$$

where x^i and y^i are the displacements of the ith particle at time t in the x and y directions, respectively. The iterated time step for the dispersed phase is determined by the maximum particle velocity at the previous time step.

To elucidate the formation features of inclusion-driven macrosegregation in the industrial steel ingots, a series of simulations of the current 3-ton bearing steel ingot with various inclusion dimensions and numbers were carried out. The half ingot is simulated owing to its geometric symmetry. In terms of the computational accuracy, a fine grid with 6×6 mm is used. The bearing steel is simplified as a five-component system of Fe-1.0 C-0.25 Si-1.5 Cr-0.35 Mn (wt pct). Based on the experiments and thermodynamic calculations, the boundary conditions and main thermo-physical parameters are listed in Tables III and IV. It is worth noting that the secondary dendrite arm

Table III. Main Physical Parameters in the Simulations of 3-Ton Bearing Steel Ingots

Symbol	Unit	Value
ρ	kg m^{-3}	7000[a]
$\rho_{Al_2O_3}$	kg m^{-3}	3640[39]
$\rho_{Ce_2O_2S}$	kg m^{-3}	6000[29]
T_m	K	1805[8]
ΔH	J kg^{-1}	2.71×10^5[8]
C_p	J kg^{-1} K^{-1}	807[a]
λ	W m^{-1} K^{-1}	33[a]
β_T	K^{-1}	1.07×10^{-4}[8]
μ_l	Pa s	4.2×10^{-3}[8]

		C[11]	Si[11]	Mn[11]	Cr[11]
k	1	0.34	0.59	0.75	0.76
m	K wt pct^{-1}	-78	-17.1	-3.32	-2.61
β_C	Wt pct^{-1}	0.011	0.0119	0.00192	-0.00397

[a]It indicates that the value is calculated by software package ProCAST[40]

Table IV. The Initial and Thermal Conditions in the Simulations of 3-Ton Bearing Steel Ingots

Material/Property	ρ (kg m^{-3})	C_P (J kg^{-1} K^{-1})	λ (W m^{-1} K^{-1})	T_0 (K)
Iron Mold	7000	800	0.29	373
Insulation Sleeve	600	1130	0.2	373
Covering Flux	210	400	0.18	373
Interfacial Heat Transfer Coefficient (W m^{-2} K^{-1})	ingot and covering flux: 300			
	ingot and sand mold: 2000			
	ingot and insulation sleeve: 200			
	covering flux and air: $5 + 4 \times 5.67 \times 10^{-8} \times 0.5 \times T^3$			
	sand mold and air: $10 + 4 \times 5.67 \times 10^{-8} \times 0.9 \times T^3$			

(a) No inclusion **(b)** d_p = 5 μm **(c)** d_p = 10 μm **(d)** d_p = 20 μm **(e)** d_p = 30 μm **(f)** d_p = 50 μm
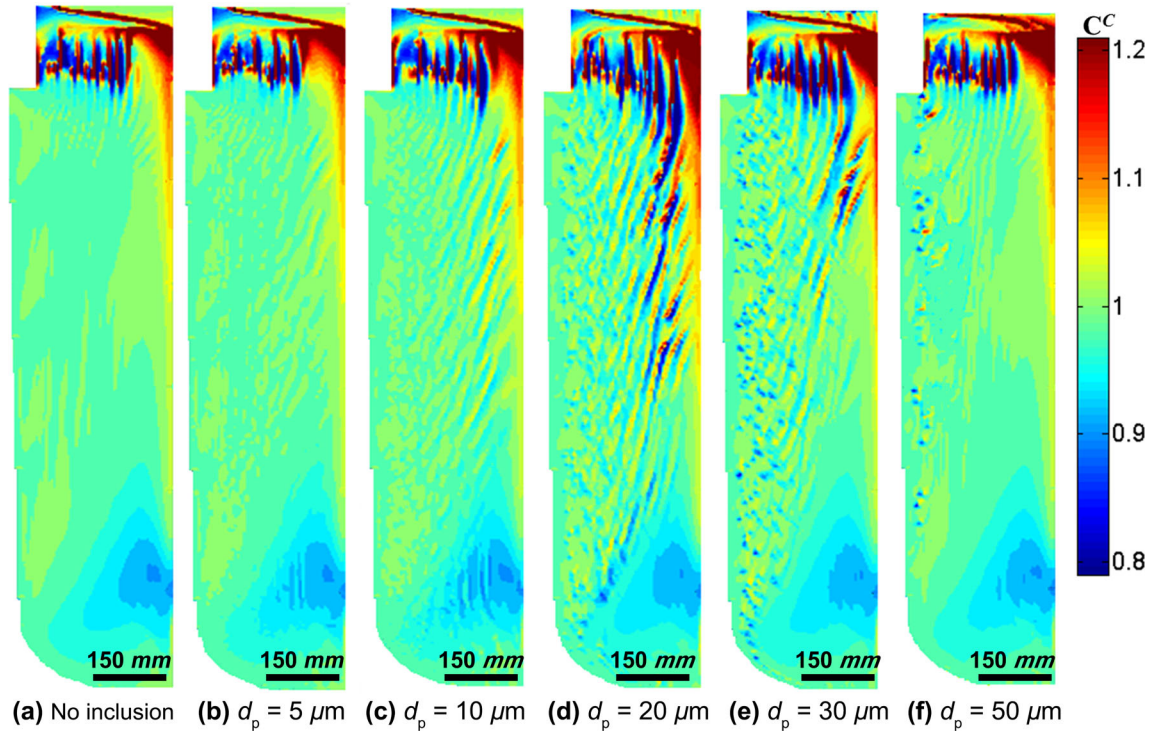
Fig. 8—The effect of Al$_2$O$_3$ size on the final carbon distribution, and the initial inclusion number is 10,000.

spacing (d_s) is not arbitrary and should be given from the experimental or calculated results, which was always neglected in the previous simulations of macrosegregation. In this study, it is calculated based on the following expression[35]:

$$d_s = 10^{-6} \times 123\varepsilon^{-0.33} \exp^{\left(-0.281C^C + 0.175C^{Mn} - 0.063C^{Cr} - 0.136C^{Mo} - 0.091C^{Ni}\right)}.$$

[22]

From Eq. [22], to calculate the value of d_s, cooling rate ε is required to be obtained by the following steps: (1) to pre-simulate the temperature field and (2) to extract and average the cooling rate of all the positions with f_s = 0.5 in the whole ingot body. Under the current solidification conditions, the cooling rate in the ingot body varies from 0.0023 to 5.5 K/s, and the calculated average value is approximately 0.011 K/s, and thus the corresponding value of d_s is about 400 μm.

IV. RESULTS AND DISCUSSION

A. *The Influences of Inclusion Size and Quantity on Macrosegregation*

Figure 8 shows the effect of Al$_2$O$_3$ sizes on the final carbon macrosegregation after complete solidification of RE-free steel, in which cases the initial total inclusion number n_0 in the whole ingot is fixed as 10,000. When the effect of alumina on convection and solidification is not considered, the channel segregation in the ingot body disappears, see Figure 8(a), but the positive segregation in the top and the negative segregation at the bottom of the ingot can be reproduced. In the riser, because of the sudden changes of insulation conditions, dimension and shape from ingot body to the riser, the local convection instability occurs, and consequently the solidification mode of mushy destabilization is triggered. Obviously, the above mushy deformation induced by the
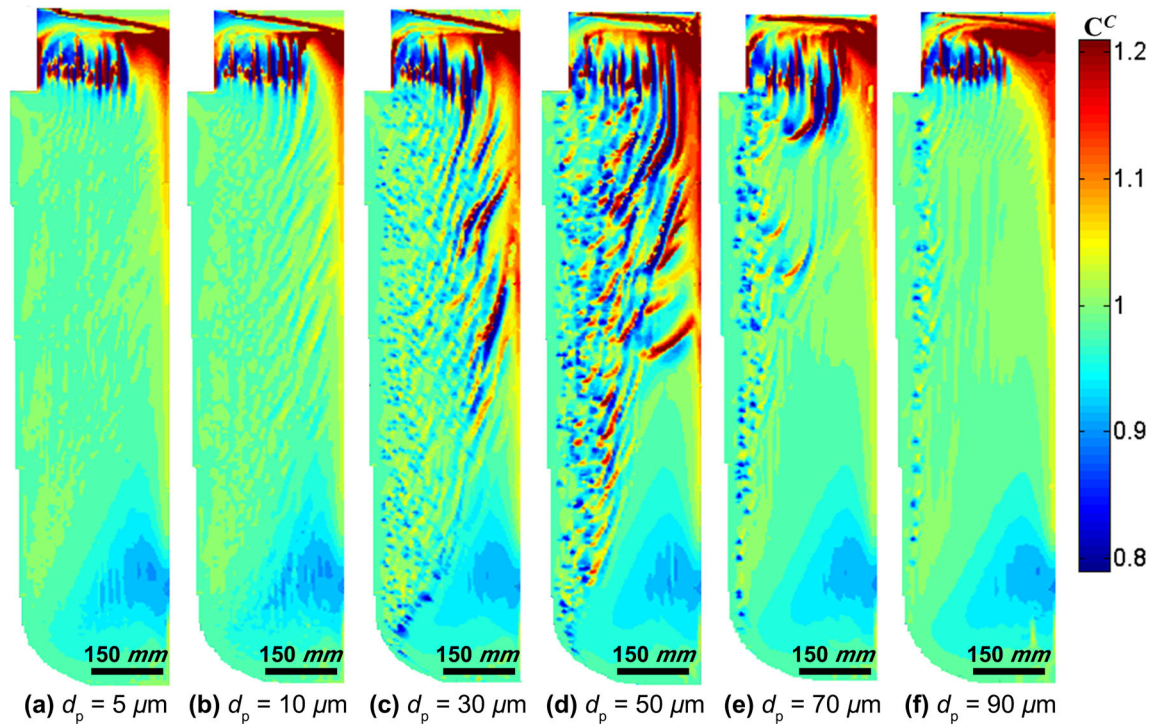
Fig. 9—The effect of Ce$_2$O$_2$S size on the final carbon distribution, and the initial inclusion number is 10,000.

thermal boundary is the origin to cause the channel or stripe segregation at the conjunction between ingot body and riser.

According to Figure 8, an appropriate range of 5–50 μm is necessary to induce the formation of channel segregation in RE-free steel. When the inclusion size is very small, such as $< 5 \mu$m, its velocity is rather tiny based on the Stokes law because the final balance velocity of inclusion particle is proportional to its square of diameter. Hence, the local melt convection and flow cannot be disturbed effectively. Actually, the inclusion particle will float with the current of melt when the interaction between inclusion and steel melt is considered. On the other hand, when the inclusion particle is large enough ($> 50 \mu$m), it will float and arrive to the top of ingot quickly. Owing to the transient interaction between the particles and melt, the turbulence tends to fade and the mushy destabilization cannot last for a long time, so no macro-scale channel segregation forms.

By contrast, the channel segregation induced by Ce$_2$O$_2$S is shown in Figure 9. It reveals that, in the RE steel ingot, the size of Ce$_2$O$_2$S inclusion ($n_0 = 10000$) to induce channel segregation is elevated from 5–50 μm to 10–90 μm due to its large density. This can also be explained roughly from Stokes law. To reach the same final critical velocity, the product of density difference and the square of particle diameter, $\left(\rho - \rho_p \right) \times d_p^2$, should be equal in both RE-free and RE steel melts. Thus, the critical Al$_2$O$_3$ sizes of 5 and 50 μm are required to be elevated to 10 and 90 μm for Ce$_2$O$_2$S particle, respectively. It indicates the importance to control large inclusions in RE-added steels in practice.

Fortunately, based on the above experimental determination, the inclusion size in RE steel will be obviously decreased, and hence there is no risk of the formation of channel segregation in the RE steel ingot according to the current simulation results.

On the other hand, the quantity of inclusion particles is the other key factor to induce channel segregation. Figure 10 shows the final carbon macrosegregation with an initial total number n_0 of Al$_2$O$_3$ particles ranging from 100 to 50,000 in the whole ingot, where the inclusion diameter is fixed as 30 μm. When the number of Al$_2$O$_3$ particles is less than 5000, channel segregation cannot be reproduced as shown in the case of inclusion-free in Figure 8(a). As it is larger than 5000, channel segregations appear, but their evolution trend is almost the same except for the channel number, length, and severity. The obvious difference is the segregation severity within the channel. With the increase in the inclusion number n_0 from 5000 to 50,000, the maximum carbon concentration within the channels varies from 1.16 to 1.67 wt pct. It is caused by the stronger and longer interaction between inclusions and the surrounding melt during solidification. On one hand, more inclusions can provide more potential sites to trigger channel segregation, and these micro-channels can be further developed with the help of other existing inclusions along the development path of microsegregation, consequently forming the macro-channel segregation. On the other hand, when the inclusion is increased, the accumulation and aggregation phenomenon of inclusions becomes more pronounced. Hence, the particle cluster will strengthen the local melt flow during
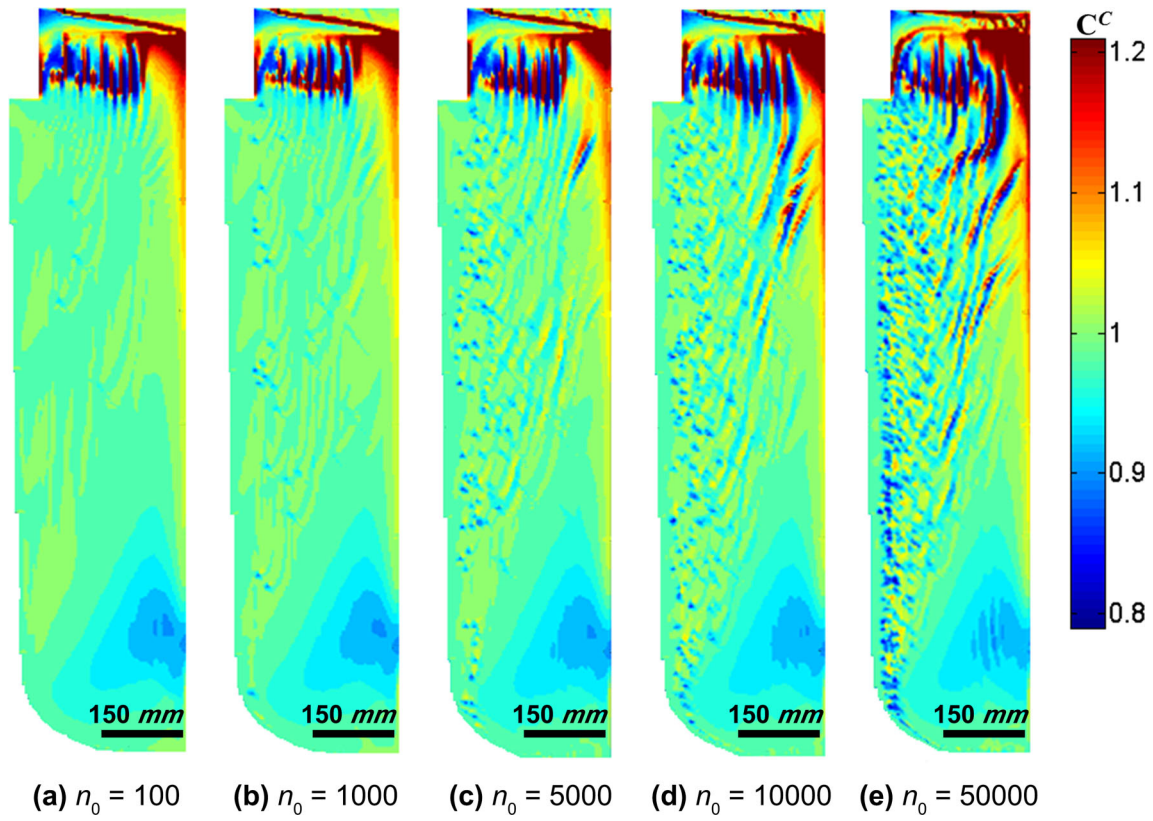
(a) n_0 = 100   **(b)** n_0 = 1000   **(c)** n_0 = 5000   **(d)** n_0 = 10000   **(e)** n_0 = 50000

Fig. 10—The effect of Al_2O_3 number on the final carbon distribution, and the inclusion diameter is 30 μm.

(a) n_0 = 100   **(b)** n_0 = 1000   **(c)** n_0 = 5000   **(d)** n_0 = 10000   **(e)** n_0 = 50000
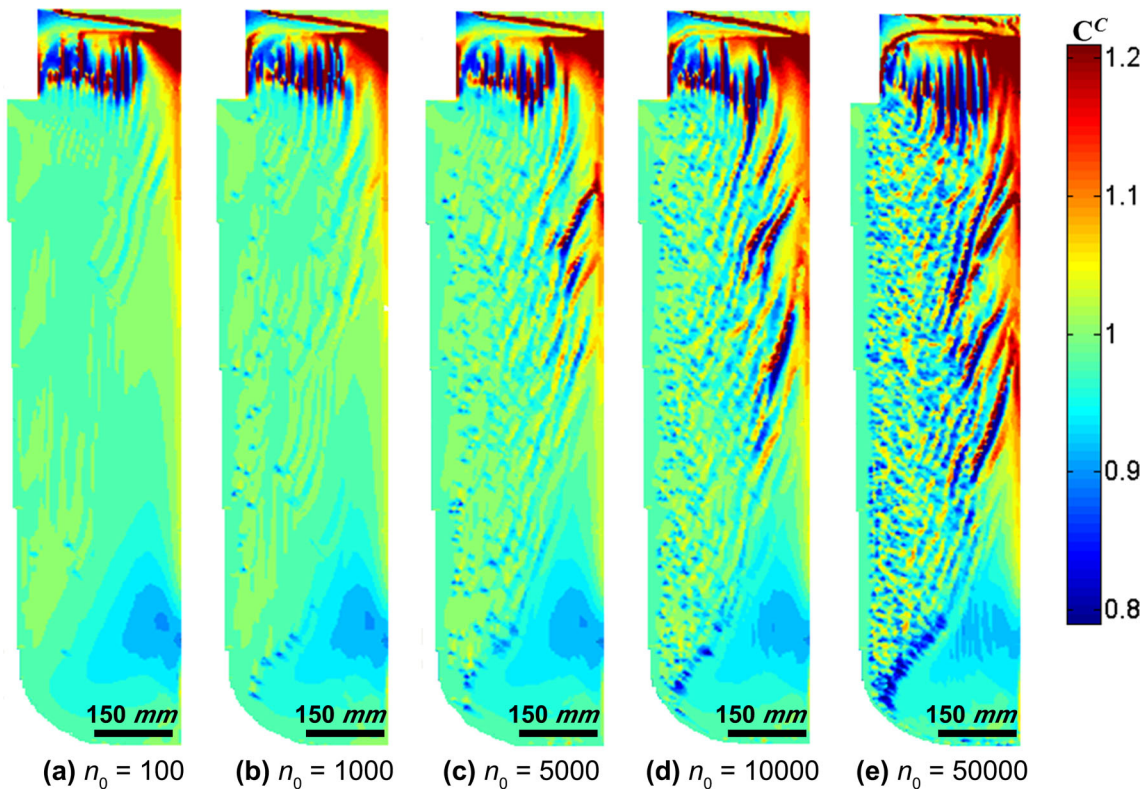
Fig. 11—The effect of Ce_2O_2S number on the final carbon distribution, and the inclusion diameter is 30 μm.

their flotation, causing more severe solute depletion or enrichment. By summarizing the volume fraction of inclusions in different cases, it is found that its critical value is about 0.015 pct.

When the Al_2O_3 particles are replaced by Ce_2O_2S inclusions, the similar characteristics of channel segregation can be observed with the increase of inclusions, as shown in Figure 11. Owing to the smaller flotation velocity and the longer action time of Ce_2O_2S (d_p = 30 μm) with the steel melt during solidification, channel segregation can grow more substantially compared with the corresponding Al_2O_3-containing steels. The simulated volume fraction of inclusions initiating the channel segregation is also at least 0.01 pct in magnitude, but its absolute value is increased to be 0.028 pct from 0.015 pct in the case of Al_2O_3-containing situation.

According to the formation theory of channel segregation by inclusion flotation in solidifying steels, the flow instability and mushy zone destabilization of steel melt have to be met to trigger the micro-channel segregation. That is, to satisfy the critical disturbance extent of steel melt in the mushy zone by inclusion motion, the same critical momentum M^{min} of particles should be reached.

$$M^{min} = n \cdot m \cdot U_p = 1/\rho \cdot V^{min} \cdot \rho_p \cdot U_p$$
$$= 1/\rho \cdot V^{min} \cdot \rho_p \cdot \frac{g d_p^2(\rho - \rho_p)}{18\mu_l} \quad [23]$$

And hence,

$$\frac{M^{min}_{Al_2O_3}}{M^{min}_{Ce_2O_2S}} = \frac{V^{min}_{Al_2O_3}}{V^{min}_{Ce_2O_2S}} \cdot \frac{\rho_{Al_2O_3}(\rho - \rho_{Al_2O_3})}{\rho_{Ce_2O_2S}(\rho - \rho_{Ce_2O_2S})} \quad [24]$$

when ρ = 7000 kg m^{-3}, $\rho_{Al_2O_3}$=3640 kgm^{-3} and $\rho_{Ce_2O_2S}$=6000 kgm^{-3} are substituted into the above formula, the following expression can be obtained.

$$V^{min}_{Ce_2O_2S} \cong 2 \cdot V^{min}_{Al_2O_3}. \quad [25]$$

Equation [25] explains why the critical volume fraction of Ce_2O_2S to stimulate the initial channel doubles that of Al_2O_3 particles. It should be noted that (1) the above expression is established when the floating spherical inclusions are able to reach a final stable velocity and the force balance is controlled by dragging force, floatation force and gravity; (2) the above requirement is to successfully trigger the initial micro-channel, but it is not adequate to cause the final formation of macro-channel, which is mainly controlled by the complex interactions among inclusion flotation, melt convection, solidification, and solute and heat transports. Consequently, once the initial micro-channel is triggered successfully, the final macro-channel induced by Ce_2O_2S is more severe than Al_2O_3 due to its long acting period between inclusions and steel melt, as shown in Figures 10 and 11.

B. The Mechanism to Reduce Macrosegregation by RE Addition

The above simulation results show that the flotation behaviors of the different inclusion types are completely different, which ultimately leads to the distinct segregation distributions. Hence, simulations are further carried out with the input of the above experimental characterization results. According to the simulation results in Section IV–A, the effective inclusion dimension to
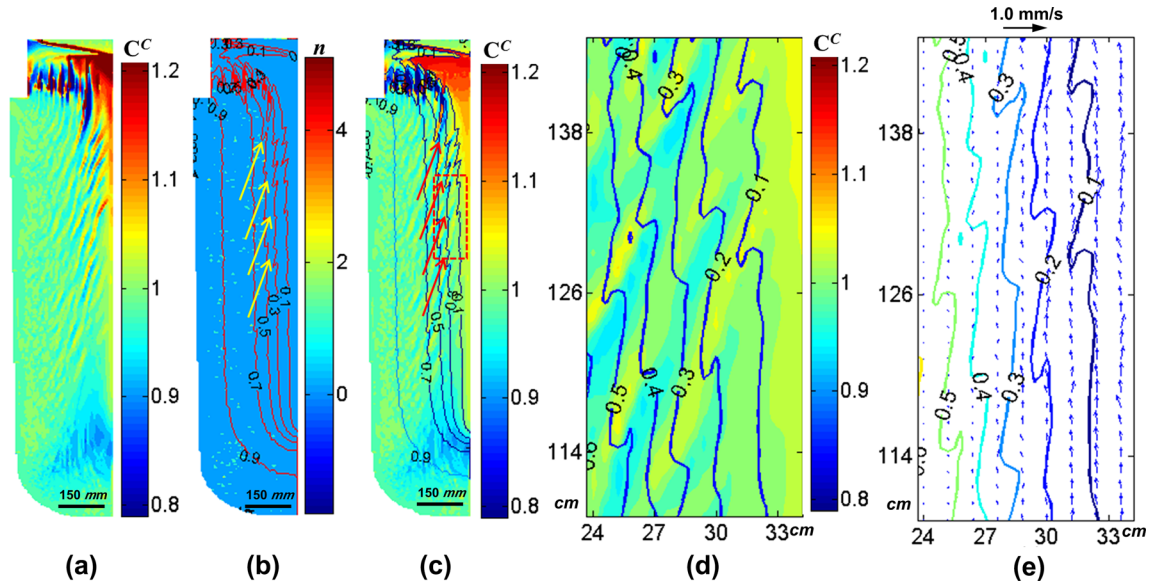

Fig. 12—The final carbon segregation (a), the whole solid fraction isolines overlaid by the inclusion distribution (b), and by the carbon concentration (c) at 5000 s, the blown-up inset of the local solid fraction isolines overlaid by the carbon concentration (d) and by flow field (e) at 5000 s marked in red box in (c) in the 3-ton RE-free steel ingot (Color figure online).

induce the formation of channel segregation is at least 5 μm, so inclusions below 5 μm are not considered in subsequent simulations. In addition, owing to much larger detection region by 2D ASPEX (50 mm^2) than 3D micro-CT (Φ800 μm $\times$ 870 μm), the inclusion information observed by the former was applied here. By summarizing the results in Tables I and II, the initial total inclusion numbers (> 5 μm) are estimated at 850 and 2200, respectively, in the RE and RE-free steel ingots based on the principle of proportionality, and their average diameters of Ce_2O_2S and Al_2O_3 are 7.5 and 10 μm, respectively.

Figure 12 shows the distribution features of the final carbon segregation, the solid fraction isolines, the inclusion distribution, and the flow field at 5000s in the RE-free steel ingot, in which most of channels are generally initiated as indicated by the yellow and red arrows in Figures 12(b) and (c), respectively. In the RE-free situation, more and larger Al_2O_3 inclusions will induce a strong flotation effect and make the local flow unstable (Figure 12(e)). The sudden increase of convection velocity or even transformation of its direction can induce the different transport modes of solute compared with the neighboring region (Figure 12(d)). It can be also found that in Figure 12(d), the enrichment and depletion of carbon solute often appear in pairs to maintain the conservation of solutes. Consequently, destabilization in the mushy zone can occur and the solid fraction isolines become locally wavy rather than flat, as shown in Figures 12(d) and (e).

Actually, the sudden acceleration of flow velocity will suppress the local isotherm velocity manifested in distorting the mush shape. Such flow perturbation may result from the sufficiently strong thermo-solutal

buoyancy or the inclusion flotation. In the current case, it is caused by the latter. But in the common model alloys such as Sn–Pb, Sn–Bi, Al–Cu, Ga–In, and Ni-based superalloy, the former is the main potential driving force.[36] Then, the flow will become stronger because of the larger permeability resulting from the relatively low solid fraction or even remelting. This phenomenon can be validated by the increasing velocity at the locations with the lower solid fraction as shown in Figure 12(e). In such situation, the flow instability can last, accompanying the advancement of the solidification front. As a consequence of the stable and successive mushy destabilization caused by the interaction between inclusion flotation, melt flow, and solidification, the macro-scale channel segregation forms eventually as is illustrated in Figure 12(a). It is worth noting that, based on the flow dynamics, the inclusions also always find their way to adapt to the local liquid fraction to choose a path with the least hydrodynamic resistance. It can be proved by combining the simulation results of inclusion distribution, liquid velocity, and solid fraction isolines surrounding the channel. That is, the local increment of liquid velocity (Figure 12(e)) and the accumulation of inclusions (Figure 12(b)) can be observed near the channel, where the solid fraction is smaller and its solidification time is longer and hence solute is enriched. Finally, with the development of the channel segregation, the coexistence phenomenon of inclusions and segregated solutes occurs, see Figures 12(b) and (c).

It should be stressed that, though the total oxygen content is as low as 4.7 ppm (see Figure 3), channel segregation still forms in the current simulation (Figure 12(a)). It is because besides inclusion-driven flotation, the thermo-solute buoyancy induced by the
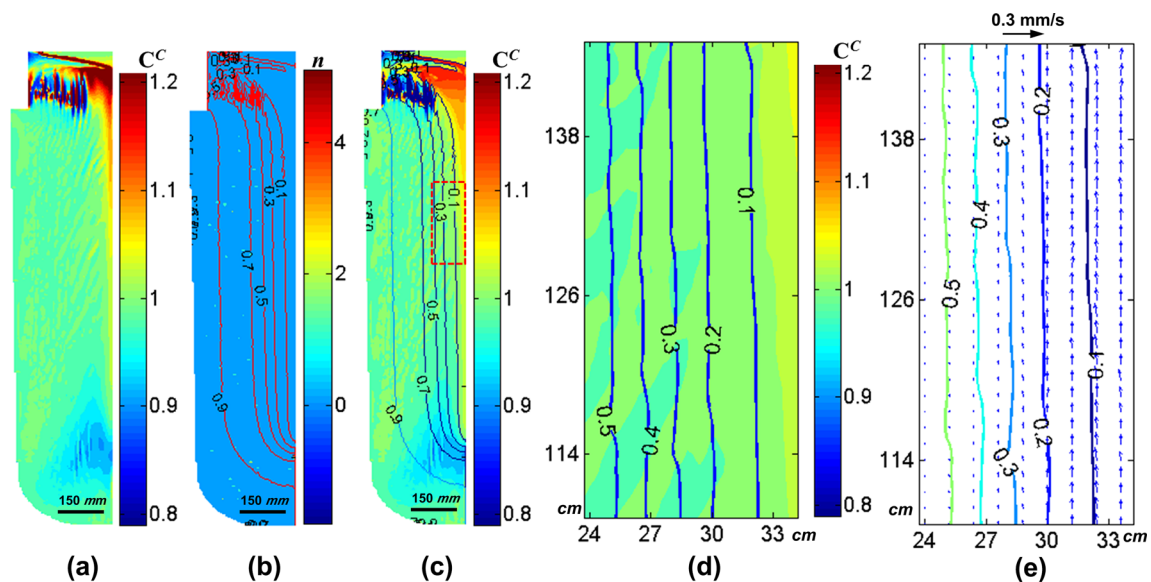

Fig. 13—The final carbon segregation (*a*), the whole solid fraction isolines overlaid by inclusion distribution (*b*) and by carbon concentration (*c*) at 5000 s, the blown-up inset of the local solid fraction isolines overlaid by carbon concentration (*d*) and by flow field (*e*) at 5000 s marked in red box in (c) in the 3-ton RE steel ingot (Color figure online).

ultra-high carbon content (normal composition is 1 wt pct) in the bearing steel is also significant. When the carbon content increases, the density difference between the mushy zone and the bulk liquid becomes larger and hence the natural convection is stronger, which obviously increases the driving force of mush destabilization and channel formation. Actually, the oxygen criterion of 10 ppm to induce channel segregation proposed by Reference 14 is more appropriate in low carbon and low alloy steels.

By contrast, in the RE steel ingot, since both the quantity and size of inclusions are reduced, the flow instability is not easy to be triggered owing to its weak driving force and perturbation on the local melt (Figure 13(e)). Meanwhile, the enrichment and segregation phenomenon of inclusions almost disappears in Figure 13(b), which causes the negligible disturbance on the local flow, solute transport, and mush shape. This is totally different from that in Figure 12(b). By comparing the flow field in the solidification front in Figures 12(e) and 13(e), the flow velocity becomes much weaker after RE addition considering the distinctly small arrow icon of 0.3 mm/s. The solidification thus progresses normally and stably as shown by the flat solid fraction isolines in Figures 13(b) and (c), and thus the carbon concentration becomes more uniform (Figure 13(d)). Quantitatively, the distribution range of carbon decreases to [0.95, 1.02] from [0.9, 1.06] after RE treatment by comparing Figures 12(d) and 13(d). Through the current simulation results, it can be concluded that the RE addition can weaken the mushy destabilization, thereby reducing and even eliminating channel segregation (Figure 13(a)).

Besides the effect of RE addition on the channel segregation, other segregation extents are listed in Figure 14, where GM, S^+, and S^- stand for the global, maximum positive, and negative segregations in the ingot body, respectively. Below are their expressions.

$$\text{GM} = 100 \cdot \frac{1}{C_0} \left[\frac{1}{V_{\text{ingot body}}} \iint\int_{V_{\text{ingot body}}} (C - C_0)^2 \mathrm{d}V \right]^{1/2}$$
[26]

$$S^+ = \max\left(C_0 - C_{\text{ingot body}}\right), \quad C_{\text{ingot body}} < C_0 \quad [27]$$

$$S^- = \max\left(C_{\text{ingot body}} - C_0\right), \quad C_{\text{ingot body}} > C_0 \quad [28]$$

It shows that all the global, positive, and negative macrosegregation (chemical inhomogeneity) in the ingot body can be reduced effectively by RE addition. It is mainly caused by the different convection intensities in the mushy zone during solidification. When channel segregation is initiated ($t = 5000$s), the maximum velocity in the mushy zone ($0.05 < f_s < 0.95$) of RE steel are decreased from 0.508 to 0.154 mm/s compared with the RE-free steel.
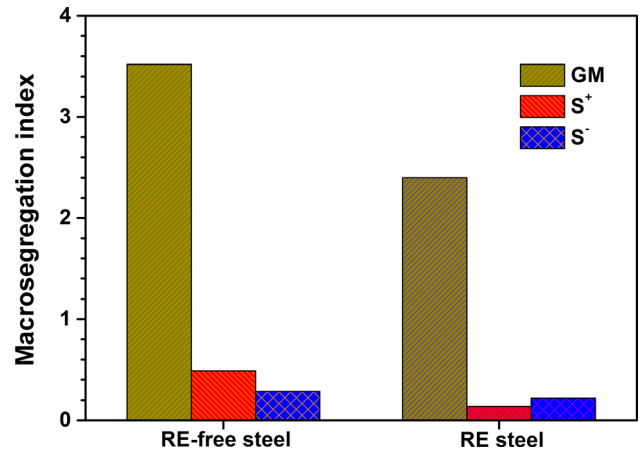

Fig. 14—The comparison of the typical macrosegregation index in the RE and RE-free steels.

C. The Critical Oxygen Content to Homogenize the Steel After RE Addition

According to the above simulation results and inclusion flotation-driven segregation theory, oxygen content and oxide play an essential role in the final segregation extent. The higher the oxygen content is, the more severe the channel segregation becomes. Our previous research has revealed that the critical total oxygen content [T.O] inducing the formation of channel segregation in widely applied Al-deoxidation steels is about 10 ppm based on the numerous dissection experiments and statistical analysis.[14,37] How will the critical value change when RE is added in steels?

When Al_2O_3 is completely modified into Ce_2O_2S by RE addition, the inclusion weight per unit mass steel at room temperature can be expressed below.

$$\frac{[T \cdot O] - [O]}{M_O / M_{Ce_2O_2S}} = \frac{1}{\rho_{\text{steel}}} \times V_{Ce_2O_2S} \times \rho_{Ce_2O_2S}, \quad [29]$$

where [O] is the dissolved oxygen; M is the molar mass and V is the volume fraction of inclusions. When [O] ≈ 0 wt pct,[38] $M_O = 32$, $M_{Ce_2O_2S} = 344$, $\rho_{\text{steel}} = 7826\,\text{kg}\,\text{m}^{-3}$ and $\rho_{Ce_2O_2S} = 6000\,\text{kg}\,\text{m}^{-3}$, the critical value of $V_{Ce_2O_2S}$ to induce channel segregation is 0.028 pct, and accordingly the total oxygen content is approximately 20 ppm. It indicates that in RE steel, the critical oxygen content initiating channel segregation is obviously elevated, which means that channel segregation is not easy to be formed at the same oxygen level compared with that of RE-free steels. Excitingly, the oxygen content will be reduced by RE treatment in practice (see Figure 3), and it is totally feasible to homogenize steels by RE addition.

D. Validation of RE Addition to Reduce Macrosegregation in Widely Used Steels

The positive effect of RE addition on the final macrosegregation is further verified and applied in the

production of two 9.5-ton 18CrNiMo17-6 gear steel ingots and two 100-ton 20Mn shaft steel ingots. They are produced by EF + LF + VD + vacuum pouring and by EF + LF + VD + pouring in air, respectively. Compared with the RE-free steels, high-pure 180 ppm La and Ce metals were added to the RE steels of 9.5-ton and 100-ton ingots. To determine the final macrosegregation extent, the 100-ton ingots were transversely dissected along the top riser line. In terms of the 9.5-ton ingot, the top riser line-section, half height-section, and the bottom cone-section were all transversely sliced. After being ground, the drill cuttings with the uniform spacing of 100 mm along the radial direction in each slice were collected for composition determination. Considering the symmetry of round 9.5-ton and 100-ton steel ingots, half of each slice was drilled and analyzed.

The final relative carbon segregations in RE-free and RE steels are interpreted in Figure 15. In 100-ton RE steel ingot, the maximum relative positive and negative segregations along the riser line decrease to 0.61 and − 0.015 from 0.75 and − 0.06, respectively. Similarly, in 9.5-ton RE steel, they are lowered to 0.22 and − 0.17 from 0.31 and − 0.19, respectively. Actually, the carbon segregations in all three slices of 9.5-ton RE steel ingot show a decreasing tendency, which contributes to the whole chemical homogeneity by RE treatment. Quantitatively, the global macrosegregation extent GM in the 9.5-ton and 100-ton RE steels are 11.3 and 20, respectively, both of which are much smaller than 14.6 and 40.2 of two RE-free steels. Both the current experimental data and simulation results reveal that, in widely used steels, the macrosegregation extent can be reduced significantly by RE treatment, which is mainly caused by jointly lowering the oxygen content and effectively modifying the inclusion number, size, composition, and morphology.

V. CONCLUSIONS

A series of experimental characterizations of inclusions by SEM, TEM, ASPEX, and 3D CT techniques were carried out to elucidate the effect of RE addition on macrosegregation in solidifying steels. After the mischmetal treatment, the maximum diameter of inclusions is decreased obviously from 26.1 to 9.2 μm, and the quantity of large inclusions (> 1 μm) is only one-third of that in RE-free steel. Most of inclusions are modified to the soft, dispersed, and spherical Ce_2O_2S (or La_2O_2S) from the hard and complex Al_2O_3-based type. Also encouraging is the fact that the total oxygen content, a key parameter influencing macrosegregation especially channel segregation, is further lowered to 4.7 from 5.5 ppm. The current characterizations reveal that RE addition will be beneficial to the reduction of macrosegregation due to the concurrent decease of oxygen content and large inclusions.

In addition, based on the multi-component/multi-phase macrosegregation model and simulation, it shows that sufficient inclusions with appropriate size can alter the local convection and trigger the mush destabilization rather than the successive solidification, consequently initiating the channel segregation in 3-ton bearing steel ingots. Owing to the larger density of Ce_2O_2S than the common oxide-based inclusions, more inclusions with a size of 10–90 μm are required to sufficiently disturb the local steel melt and induce the formation of micro-channel, and the critical fraction of inclusions to initialize the channel increases to 0.028 from 0.015 pct of RE-free steel. But, the fact is that these large-size inclusions become less *via* RE addition due to its smaller interfacial tension with steel melt and lower oxygen content. Meanwhile, the expected inclusion modification with smaller size and number causes the weaker interdendritic convection in RE steel, thereby
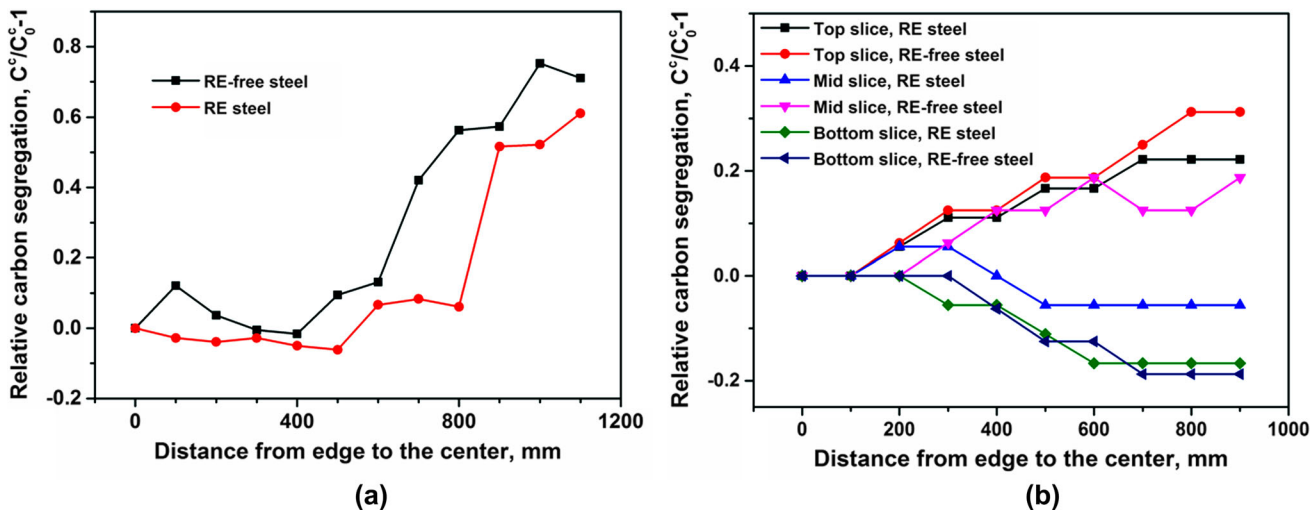

Fig. 15—The comparison of the relative carbon segregation in 100-ton (*a*) and 9.5-ton (*b*) steel ingots after RE addition.

reducing the extent of other macrosegregation types such as positive and negative segregations. Additionally, the critical oxygen content to induce channel segregation *via* RE treatment is sharply elevated to 20 ppm, which effectively lowers the risk of channel formation. Finally, the novel finding to reduce macrosegregation by RE addition has been further verified successfully and extended to the larger 9.5-ton and 100-ton steel ingots. This study provides a common and innovative method to control macrosegregation and to fabricate homogenized steels *via* RE addition.

ACKNOWLEDGMENTS

CONFLICT OF INTEREST

On behalf of all authors, the corresponding author states that there is no conflict of interest.

OPEN ACCESS

NOMENCLATURE

C_l, C_s, C	Liquid, solid, and mixture concentrations (wt pct)
$h_s, h_l, H,$	Solid, liquid, and mixture enthalpies (J kg^{-1})
ΔH	Latent heat (J kg^{-1})
C^*	Reference concentration (wt pct)
T^*	Reference temperature (K)
u_p, v_p	Particle velocity components in x and y directions (m s^{-1})
u, v	Liquid velocity components in x and y directions (m s^{-1})
$\overline{u_p}, \overline{v_p},$	Average particle velocities in x and y directions (m s^{-1})
f_s, f_l	Fractions of solid and liquid
$\overrightarrow{U}$	Superficial velocity (m s^{-1})
$\overrightarrow{U_l}$	Liquid velocity (m s^{-1})
λ	Heat conductivity (W m^{-1} K^{-1})
c_p	Specific heat (J kg^{-1} K^{-1})
μ_l	Liquid dynamic viscosity (pa s)
$\vec{g}$	Acceleration of gravity (m s^{-2})
t	Time (s)
n	Particle number
m	Liquidus slope (K wt pct^{-1})
T_l, T_m	Liquidus of steel and melting point of solvent (K)
d_s	Secondary dendritic arm spacing (μm)
K	Partition coefficient
f_p	Area fraction of inclusion
β_T	Thermal expansion coefficient (K^{-1})
β_C	Compositional expansion coefficient (wt pct^{-1})
Re	Relative Reynolds number
ρ, ρ_p	Densities of steel and inclusion (kg m^{-3})
P	Pressure (pa)
d_p	Particle diameter (m

SUBSCRIPTS AND SUPERSCRIPTS

s, l	Solid and liquid phases
p	Inclusion particle
i	The ith inclusion particle
j	The jth solute element
sl, pl	Interaction between liquid and solid or inclusion

REFERENCES

1. S. Karagadde, L. Yuan, N. Shevchenko, S. Eckert, and P.D. Lee: *Acta Mater.*, 2014, vol. 79, pp. 168–80.
2. L. Yuan and P.D. Lee: *Acta Mater.*, 2012, vol. 60, pp. 4917–26.
3. M. Wu and A. Ludwig: *Acta Mater.*, 2009, vol. 57, pp. 5621–31.
4. F.L. Ren, H.H. Ge, D.X. Cai, J. Li, Q.D. Hu, M.X. Xia, and J.G. Li: *Metall. Mater. Trans. A*, 2018, vol. 49A, pp. 6243–54.
5. N. Ren, J. Li, C. Panwisawas, M.X. Xia, H.B. Dong, and J.G. Li: *Acta Mater.*, 2021, vol. 206, p. 116620.
6. N. Ren, C. Panwisawas, J. Li, M.X. Xia, H.B. Dong, and J.G. Li: *Acta Mater.*, 2021, vol. 215, p. 117043.
7. J. Li, M. Wu, A. Ludwig, and A. Kharicha: *Int. J. Heat Mass Transfer*, 2014, vol. 72, pp. 668–79.
8. H. Combeau, M. Zaloznik, S. Hans, and P. Richy: *Metall. Mater. Trans. B*, 2009, vol. 40B, pp. 289–304.
9. M. Ahmadein, M. Wu, and A. Ludwig: *J. Cryst. Growth*, 2015, vol. 417, pp. 65–74.
10. T. Koshikawa, M. Bellet, C.-A. Gandin, H. Yamamura, and M. Bobadilla: *Acta Mater.*, 2017, vol. 124, pp. 513–27.
11. M.C. Schneider and C. Beckermann: *Metall. Mater. Trans. A*, 1995, vol. 26A, pp. 2373–88.
12. E.J. Pickering: *ISIJ Int.*, 2016, vol. 53, pp. 935–49.
13. C. Beckermann: *Int. Mater. Rev.*, 2002, vol. 47, pp. 243–61.

14. D. Li, X.-Q. Chen, P. Fu, X. Ma, H. Liu, Y. Chen, Y. Cao, Y. Luan, and Y. Li: *Nat. Commun.*, 2014, vol. 5, p. 5572.
15. K.A. Gschneidner: *Industrial Applications of Rare Earth Elements*, ACS, Washington, 1981, pp. 43–78.
16. Y.M. Wu, L.M. Wang, and T. Du: *J. Less common Met.*, 1985, vol. 110, pp. 187–93.
17. Y. Nuri, T. Ohashi, T. Hiromoto, and O. Kitamura: *Tetsu to Hagane*, 1980, vol. 66, pp. 618–27.
18. T.Y. Hsu: *ISIJ Int.*, 1988, vol. 38, pp. 1153–64.
19. M. Boccalini Jr., A.V.O. Corrêa, and H. Goldenstein: *Mater. Sci. Technol.*, 1999, vol. 15, pp. 621–26.
20. J. Hufenbach, A. Helth, M.-H. Lee, H. Wendrock, L. Giebeler, C.-Y. Choe, K.-H. Kim, U. Kuhn, T.-S. Kim, and J. Eckert: *Mater. Sci. Eng. A*, 2016, vol. 674, pp. 366–74.
21. L.A. Smirnov, V.A. Rovnushkin, A.S. Oryshchenko, G. Yu Kalinin, and V.G. Milyuts: *Metallurgist*, 2016, vol. 59, pp. 1053–61.
22. Z. Adabavazeh, W.S. Hwang, and Y.H. Su: *Sci. Rep.*, 2017, vol. 7, p. 46503.
23. X. Jiang and S.H. Song: *Mater. Sci. Eng. A*, 2014, vol. 613, pp. 171–77.
24. S.-T. Kim, S.-H. Jeon, I.-S. Lee, and Y.-S. Park: *Corros. Sci.*, 2010, vol. 52, pp. 1897–1904.
25. S.R. Stock: *Int. Mater. Rev.*, 1999, vol. 44, pp. 141–64.
26. S.R. Stock: *Int. Mater. Rev.*, 2008, vol. 53, pp. 129–81.
27. N. Limodin, J. Rethore, J.-Y. Buffiere, A. Gravouil, F. Hild, and S. Roux: *Acta Mater.*, 2009, vol. 57, pp. 4090–4101.
28. Y.F. Cao, Y. Chen, and D.Z. Li: *Acta Mater.*, 2016, vol. 107, pp. 325–36.
29. P.E. Waudby: *Int. Metal. Rev.*, 1978, vol. 23, pp. 74–98.
30. C.Y. Yang, Y.K. Luan, D.Z. Li, and Y.Y. Li: *J. Mater. Sci. Technol.*, 2019, vol. 35, pp. 1298–1308.
31. G.K. Sigworth and J.F. Elliott: *Metal Sci.*, 1974, vol. 8, pp. 298–310.
32. Y.F. Cao, Y. Chen, P.X. Fu, H.W. Liu, and D.Z. Li: *Metall. Mater. Trans. A*, 2017, vol. 48A, pp. 2260–73.
33. D. Gidaspow: *Multiphase Flow and Fluidization: Continuum and Kinetic Theory Description*, Academic Press, New York, 1994, p. 35.
34. D.R. Liu, B.G. Sang, X.H. Kang, and D.Z. Li: *Metall. Mater. Trans. B*, 2011, vol. 42B, pp. 210–23.
35. J. Miettinen, S. Louhenkilpi, H. Kytonen, and J. Laine: *Math. Comput. Simul.*, 2010, vol. 80, pp. 1536–50.
36. Y.F. Cao, Y. Chen, D.Z. Li, H.W. Liu, and P.X. Fu: *Metall. Mater. Trans. A*, 2016, vol. 47A, pp. 2927–39.
37. Y.F. Cao, D. Li, X.-Q. Chen, C. Liu, Y. Chen, P. Fu, H. Liu, X. Ma, Y. Liu, and Y. Luan: *Mater. Des.*, 2021, vol. 205, p. 109723.
38. C. Barouh, T. Schuler, C.-C. Fu, and M. Nastar: *Phys. Rev. B*, 2014, vol. 90, p. 054112.
39. H. Shibata, D.R. Poirier, and T. Emi: *ISIJ Int.*, 1998, vol. 38, pp. 339–47.
40. ProCAST v14 package, ESI Group, Paris, France.

Publisher's Note Springer Nature remains neutral with regard to jurisdictional claims in published maps and institutional affiliations.